

Direct determination of the neutron skin thicknesses in $^{40,48}\text{Ca}$ from proton elastic scattering at $E_p = 295$ MeV

J. Zenihiro,^{1,*} H. Sakaguchi,² S. Terashima,³ T. Uesaka,¹ G. Hagen,^{4,5} M. Itoh,⁶ T. Murakami,⁷ Y. Nakatsugawa,⁸ T. Ohnishi,¹ H. Sagawa,^{1,9} H. Takeda,¹ M. Uchida,¹⁰ H.P. Yoshida,² S. Yoshida,¹¹ and M. Yosoi²

¹RIKEN Nishina Center, Wako, Saitama 351-0198, Japan

²Research Center for Nuclear Physics, Osaka University, Ibaraki, Osaka 567-0047, Japan

³School of Physics and Nuclear Energy Engineering, Beihang University, Beijing 100191, China

⁴Physics Division, Oak Ridge National Laboratory, Oak Ridge, Tennessee 37831, USA

⁵Department of Physics and Astronomy, University of Tennessee, Knoxville, Tennessee 37996, USA

⁶Cyclotron and Radioisotope Center, Tohoku University, Sendai, Miyagi 980-8578, Japan

⁷Department of Physics, Kyoto University, Kyoto 606-8502, Japan

⁸Institute of High Energy Physics, Chinese Academy of Sciences, Beijing 100049, China

⁹Center for Mathematics and Physics, University of Aizu, Fukushima 965-0001, Japan

¹⁰Department of Physics, Tokyo Institute of Technology, Meguro, Tokyo 152-8551, Japan

¹¹Science Research Center, Hosei University, 2-17-1 Fujimi, Chiyoda, Tokyo 102-8160, Japan

The neutron density distributions and neutron skin thicknesses in $^{40,48}\text{Ca}$ are determined from the angular distributions of the cross sections and analyzing powers of polarized proton elastic scattering at $E_p = 295$ MeV. Based on the framework of the relativistic impulse approximation with the density-dependent effective NN interaction, the experimental data is successfully analyzed, providing precise information of neutron and proton density profiles of $^{40,48}\text{Ca}$ with small uncertainties. The extracted neutron and proton density distributions give neutron skin thicknesses in $^{40,48}\text{Ca}$ for $-0.010_{-0.024}^{+0.022}$ fm and $0.168_{-0.028}^{+0.025}$ fm, respectively. The results of the density profiles and the neutron skin thickness in ^{48}Ca are directly compared with the *ab initio* coupled-cluster calculations with interactions derived from chiral effective field theory, as well as relativistic and non-relativistic energy density functional theories.

Protons and neutrons in a nucleus tend to be distributed so that their density sum does not exceed the saturation density $\rho_{\text{sat}} \sim 0.17 \text{ fm}^{-3}$. The proton and neutron distributions are almost identical; they have a plateau of density $\sim 0.5\rho_{\text{sat}}$ at the center in symmetric nuclei where the neutron number and the proton number are almost the same ($N \sim Z$). On the other hand, excess neutrons in neutron-rich nuclei are pushed to the nuclear surface, forming a region where only neutrons exist. This region is called a “neutron skin”.

Theoretical studies indicate that the thickness of the neutron skin Δr_{np} , which is defined as the difference of the neutron and proton root-mean-square (rms) radii ($\Delta r_{np} \equiv r_n - r_p$), embodies the stability of pure neutron matter. The quantity that characterizes the stability of neutron matter is called “symmetry energy”. The neutron matter equation of state (EOS) is a sum of well-known EOS of the symmetric nuclear matter and the symmetry energy. EOS governs not only the formation of nuclei but also astrophysical phenomena like neutron stars and super nova explosions. Consequently, the neutron matter EOS has been intensively studied in both nuclear physics and astrophysics [1–5]. The experimentally-measured Δr_{np} can help elucidate the nature of high-density neutron matter occurring at neutron stars and binary neutron star mergers in the universe [6].

In previous studies, the doubly magic ^{208}Pb has been used as a benchmarking nucleus because the double magicity removes the effects from a complicated nuclear structure. This enables reliable comparisons between the experimental results and theoretical predictions. Δr_{np} in ^{208}Pb is theoretically predicted to have a strong correlation with the coefficient L of the first density-derivative of the symmetry energy [7–9]. Many

facilities have made experimental efforts to determine Δr_{np} in ^{208}Pb by measuring proton elastic scattering [10, 11], coherent pion-photoproduction [12], antiprotonic atom X-ray [13], and electric dipole polarizability [14]. Their results are in the range of 0.15–0.21 fm with the error of approximately ± 0.03 fm. The PREX experiment using parity-violating (PV) electron scattering resulted in $\Delta r_{np} = 0.33_{-0.18}^{+0.16}$ fm [15], which is consistent with other results within its large statistical error. The results have been compared with theoretical predictions based on the relativistic and non-relativistic energy density functional (EDF) theories [1, 3, 16, 17].

Recently, Δr_{np} in ^{48}Ca has been investigated both theoretically and experimentally. One merit of ^{48}Ca is that the nucleus is within the range of the state-of-the-art *ab initio* calculations [18–22]. An interesting physics case is the direct assessment of the three nucleon force (3NF) effects. The 3NF plays an important role in high-density nuclear matter [23]. *Ab initio* coupled-cluster (CC) calculations based on the chiral effective field theory (EFT) interactions including the three-nucleon force, have been successfully performed for ^{48}Ca [20, 22, 24]. Δr_{np} in ^{48}Ca should exhibit a new aspect of the neutron matter EOS, which cannot be seen in ^{208}Pb because an *ab initio* calculations cannot be applied at present to ^{208}Pb . In this Letter, we present the results of the direct determination of the neutron density distribution and Δr_{np} in $^{40,48}\text{Ca}$ by proton elastic scattering at 295 MeV. The extracted neutron density distribution and Δr_{np} in ^{48}Ca are compared with recent *ab initio* CC calculations [22, 25] and predictions of relativistic and non-relativistic EDF theories.

Several experimental studies on Δr_{np} in ^{48}Ca have been performed and planned [26, 27]. The electric dipole polariz-

ability α_D of ^{48}Ca has been precisely determined by combining proton inelastic scattering data with photoabsorption data [26]. Δr_{np} in ^{48}Ca has been deduced by comparing the data with several EDF and *ab initio* theories. However, a direct determination of Δr_{np} in ^{48}Ca independent from a specific nuclear structure model is very important to examine the theory. One possibility is a CREX experiment using PV electron scattering which is a clean probe compared with hadronic probes [27]. The electro-weak interaction mediated by a photon and the Z^0 boson is used to probe neutrons inside a nucleus. The experiment is quite difficult because the precision of ppb level is required for the measurement of the PV asymmetry.

Proton elastic scattering is another approach to directly extract the neutron density distributions. Compared to PV electron scattering, the advantages are a high sensitivity to the neutron density and a highly attainable statistics due to a large cross section. The cost for the high efficiency is more complicated reaction mechanism than that in electron scattering. An accurate determination of the neutron density distribution requires an established reaction model and a reliable calibration using nuclei with a well-known density distribution.

Herein we use proton elastic scattering at ~ 300 MeV and analysis in the framework of the relativistic impulse approximation (RIA). The weakest nucleon-nucleon (NN) interaction appears around 300 MeV and the nucleus is the most transparent to an incident proton. This allows the impulse approximation to be used for the reaction analysis, providing the opportunity to determine the density distribution at the nuclear interior.

The angular distributions of the cross sections and analyzing powers for polarized proton elastic scattering from $^{40,48}\text{Ca}$ were measured with a high-resolution magnetic spectrometer, ‘‘Grand Raiden’’ [29] at Research Center for Nuclear Physics, Osaka University, over an angular range of 7° – 48° . Polarized protons accelerated to 295 MeV were scattered by a natural Ca foil (abundance of ^{40}Ca 96.9%) and an enriched ^{48}Ca foil (enrichment 97.7%) with thicknesses of 3.50 and 1.06 mg/cm 2 , respectively. Beam polarization was kept above 70% during the measurements. Beam intensity was adjusted in the range of 1–400 nA, depending on the scattering angle. The momenta of scattered protons, which were analyzed by the Grand Raiden spectrometer, were determined by the focal plane detectors. The typical energy resolution was about 100 keV in the full width at half maximum. As shown in Fig. 1, the measured data-sets of the differential cross sections and analyzing powers of $^{40,48}\text{Ca}(\vec{p}, p)$ (black dots) cover the wide momentum transfer range of 0.5–3.5 fm $^{-1}$.

The neutron density distributions are determined by the method employed in Refs [11, 30]. The method is based on the RIA model developed by Murdock and Horowitz (MH model) [31], which is among the most successful models for proton elastic scattering in the intermediate energy region (≥ 200 MeV) [30]. The present analysis modified the relativistic Love-Franey (RLF) NN interaction employed in the original MH model [32] to take the effects of the nuclear medium into account, e.g. Pauli blocking, multi-step processes, and vac-

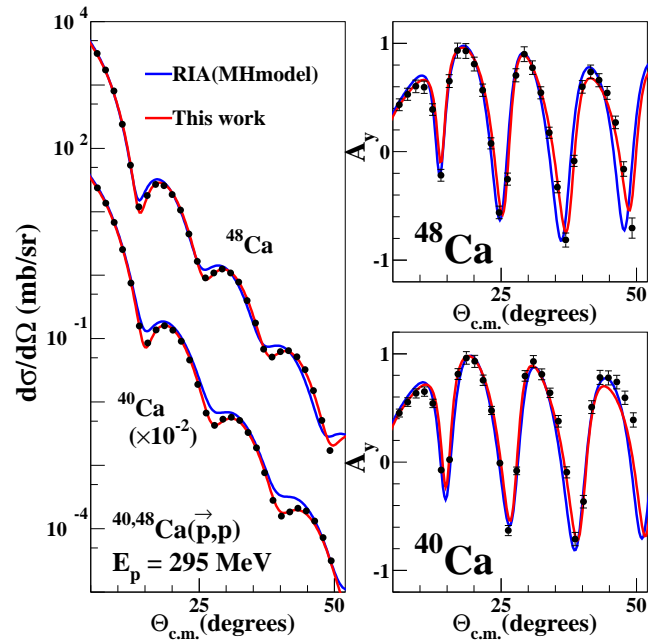


FIG. 1. Differential cross sections and analyzing powers for polarized proton elastic scattering from $^{40,48}\text{Ca}$ at 295 MeV. Blue and red lines are from the MH model and the result of the best-fit in this analysis, respectively.

uum polarization effects. The modification was introduced in a form of density-dependent coupling constants and masses of mesons used in the RLF interaction [33]. As reported in Ref. [11], the density-dependent parameters in the modification were well determined so that the medium-modified RIA calculation reproduces the proton elastic scattering data on ^{58}Ni at the same incident energy as the present work. Previous studies [11, 28] have demonstrated that the analysis method successfully works in different regions of nuclei like tin and lead. The parameters determined for ^{58}Ni work well for $A = 116$ – 208 . Thus, these parameters should be reasonable in the case of the calcium isotopes with masses closer to $A = 58$.

To single out the precise neutron density distribution $\rho_n(r)$, the point-proton density distribution $\rho_p(r)$ is necessary. The nuclear charge distribution $\rho_{ch}(r)$ was precisely determined from the electron scattering data [34]. Thus, $\rho_p(r)$ can be derived by unfolding $\rho_{ch}(r)$ with the intrinsic proton and neutron electromagnetic distributions. Using the Fourier transforms of the distributions in the momentum space q ($F_i(q) \equiv \mathcal{F}\{\rho_i(r)\} = \int \rho_i(r) \exp(i\mathbf{q} \cdot \mathbf{r}) d\mathbf{r}$), the relation can be written as

$$F_{ch}(q) = F_p(q)G_E^p(q^2) + F_n(q)G_E^n(q^2) + F_{SO}(q), \quad (1)$$

where F_{ch} , $F_{p(n)}$, and $G_E^{p(n)}$ are the nuclear charge, the point-proton (neutron), and the Sachs single-nucleon electric form factors, respectively. The value of $r_{p(n)}^2 = 0.769$ fm 2 (-0.116 fm 2) in Ref. [36] is employed for the mean-square single-proton (neutron) charge radius of $G_E^{p(n)}$. The nuclear charge distributions of $^{40,48}\text{Ca}$ were taken from Ref. [34].

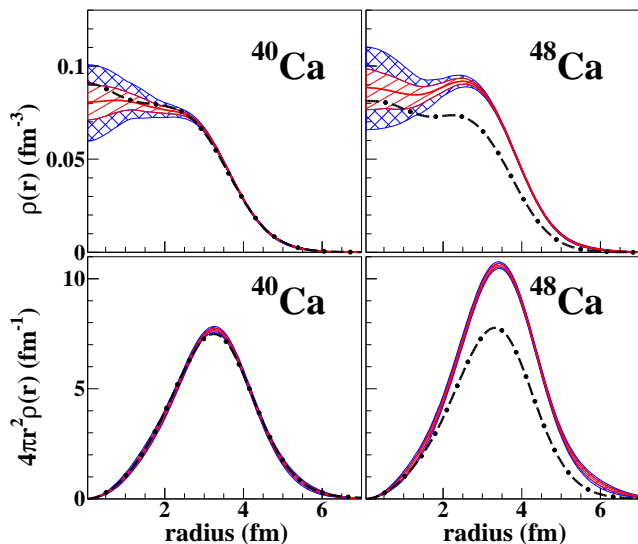


FIG. 2. Extracted ρ_n with error-envelopes of $^{40,48}\text{Ca}$ (red hatched and blue cross-hatched) and ρ_p derived from ρ_{ch} (black dash-dotted). Upper panels are the density distribution ($\rho(r)$), and the lower panels are the nucleon number distribution ($4\pi r^2 \rho(r)$).

The spin-orbit contribution F_{SO} is mainly attributed to the nucleons in an open l shell. Although its contribution to the entire proton density is quite small and neglected in many cases, it has a non-negligible effect in the determination of Δr_{np} . If $(2j+1)$ neutrons are filled in the $j = l + 1/2$ sub-shell and the proton shell is closed like ^{48}Ca , F_{SO} can be approximated as

$$F_{SO}(q) \approx \frac{l(2j+1)(G_E^n(q^2) - 2G_M^n(q^2))}{4m^2} \mathcal{F} \left\{ \frac{\partial(\rho_n^l(r))}{r^2 \partial r} \right\}, \quad (2)$$

where G_M^n is the single-neutron magnetic form factor, $\rho_n^l(r)$ is the density of each neutron in the $j = l + 1/2$ subshell, and m is the nucleon mass. (The relativistic description of F_{SO} is presented in Refs. [37, 38].) The spin-orbit contribution is sizable in ^{48}Ca due to the eight neutrons in the $f_{7/2}$ subshell. The increase of r_p in ^{48}Ca due to the F_{SO} term is evaluated to be ~ 0.02 fm [38, 39], which is compatible with the typical uncertainty of Δr_{np} [11]. Hence, the spin-orbit contribution should be included to determine ρ_p in ^{48}Ca . The F_{SO} contribution in ^{40}Ca can be neglected because the nucleons in the LS -closed shells do not contribute to the F_{SO} term, as shown in Ref. [39] for the non-relativistic limit.

The extraction of ρ_n in $^{40,48}\text{Ca}$ was carried out by a χ^2 fitting to the proton elastic scattering data with ρ_p determined by solving Eqs. (1) and (2) iteratively. ρ_n is modeled with a sum-of-Gaussian (SOG) function with 11 free parameters. There is no *a priori* assumption on the form factor and the extracted density distributions are independent of specific nuclear structure models. ρ_p is derived by applying ρ_n determined from the proton scattering data to the second and third terms in Eq. (1) and the ρ_n^l term in Eq. (2). The $(2j+1)\rho_n^l$ is approximated with $\rho_n - \rho_p$. The error of ρ_p is not considered in this fitting

TABLE I. Table of the rms radii and the skin thicknesses. r_{ch} and r_p used in this work, and the extracted r_n and Δr_{np} in $^{40,48}\text{Ca}$ are listed. δ^{exp} and $\delta^{\text{exp+mdl}}$ are the two types of errors of r_n and Δr_{np} due to the experimental errors only and the errors including model uncertainties, respectively. For ^{48}Ca , some EDF and *ab initio* predictions are compared. All values are in fm.

| | | r_{ch} | r_p | r_n | Δr_{np} | δ^{exp} | $\delta^{\text{exp+mdl}}$ |
|------------------|---------------------|----------|-------|-------|-----------------|-----------------------|---------------------------|
| ^{40}Ca | This work | 3.480 | 3.385 | 3.375 | -0.010 | $+0.022$ -0.023 | $+0.049$ -0.048 |
| ^{48}Ca | This work | 3.460 | 3.387 | 3.555 | 0.168 | $+0.025$ -0.028 | $+0.052$ -0.055 |
| | DD-MEB | - | 3.39 | 3.57 | 0.18 | - | - |
| | SAMI-J28 | - | 3.44 | 3.60 | 0.16 | - | - |
| | NNLO _{sat} | - | 3.41 | 3.54 | 0.13 | - | - |
| | Δ NNLO | - | 3.47 | 3.62 | 0.15 | - | - |

procedure since it is much smaller than that of ρ_n . The χ^2 fitting procedure started with initial values of $\rho_n = (N/Z)\rho_p$ and $F_{SO} = 0$ and continued until the self-consistent solution was obtained.

While the blue solid lines in Fig. 1 represent the predictions by the original MH model with Dirac-Hartree (DH) nucleon densities [35], the red solid lines are the best-fit results with the reduced χ^2 minima 4.6 and 4.0 for $^{40,48}\text{Ca}$, respectively. Figure 2 shows the extracted ρ_n in $^{40,48}\text{Ca}$ (red solid) together with ρ_p used in the search after the iteration (black dash-dotted). The upper panels in Fig. 2 show the density distributions, whereas the lower panels are those multiplied by the phase space factor $4\pi r^2$. The red hatched areas show the standard error envelopes due to the experimental statistical and systematic errors. The blue cross-hatched areas are shown to visualize the maximum uncertainty of the present method as well as the experimental errors. The uncertainty is attributed to any effect that makes the reduced χ^2 larger than unity and is evaluated by determining the density distributions for the same data set but with artificially increased errors so that the reduced χ^2 becomes unity. The blue cross-hatched areas are comparable to the red hatched areas. The results show that the present method is well established for the accurate determination of density distributions. More details of the analysis method are reported in Refs. [11, 30]. In ^{40}Ca , ρ_n has almost the same shape as ρ_p . On the other hand, ρ_n in ^{48}Ca is clearly enhanced over ρ_p and exhibits the characteristic nose structure around 3 fm, as shown in the top-right panel of Fig. 2. This structure is attributed to the radial distribution of the $1f_{7/2}$ orbit in which the excess eight neutrons are filled.

As listed in Table I, the neutron rms radii of $^{40,48}\text{Ca}$ result in values of $3.375^{+0.022}_{-0.023}$ fm and $3.555^{+0.025}_{-0.028}$ fm, respectively. The errors δ^{exp} in Table I correspond to the experimental error envelopes (red hatched) in Fig. 2. If error envelopes which include the model ambiguities (blue cross-hatched) are considered, the r_n values of $^{40,48}\text{Ca}$ become $3.375^{+0.049}_{-0.048}$ fm and $3.555^{+0.052}_{-0.055}$ fm, respectively. The r_p values of $^{40,48}\text{Ca}$ are 3.385 fm and 3.387 fm, respectively. If F_{SO} in Eq. (1) is not considered for ^{48}Ca , the r_p value becomes 3.371 fm. Table I lists the theoretical predictions of r_p and r_n of ^{48}Ca along with the ex-

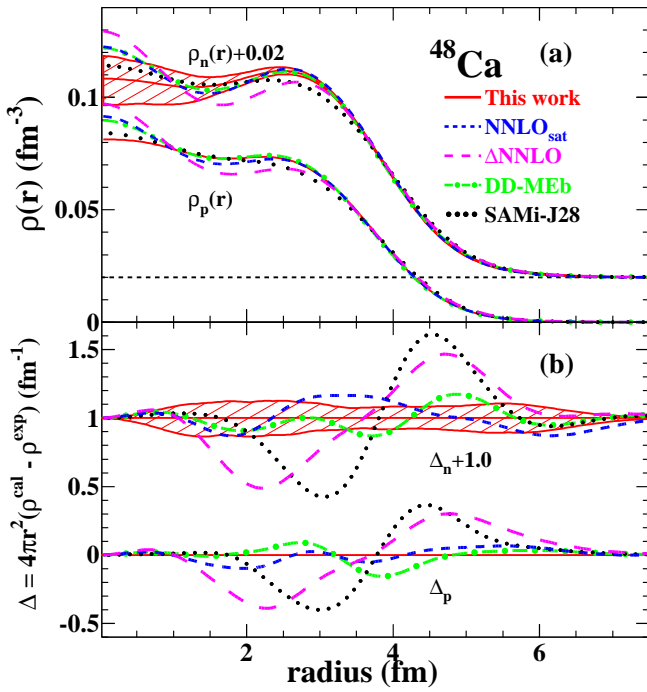


FIG. 3. (a) Extracted ρ_n and ρ_p of ^{48}Ca compared with theoretical predictions. “DD-ME δ ” (green dash-dotted) and “SAMi-J28” (black dotted) are from a relativistic and a Skyrme EDF parameterizations, respectively, while “NNLO $_{\text{sat}}$ ” (blue short-dash) and “ Δ NNLO” (magenta long-dash) are the predictions by the *ab initio* CC method. (b) Density deviation ($4\pi r^2(\rho^{\text{cal}} - \rho^{\text{exp}})$) of theories (ρ^{cal}) presented in the upper panel (a) from our work (ρ^{exp}).

perimental results: the *ab initio* CC method with NNLO $_{\text{sat}}$ and Δ NNLO interactions [20, 22], as well as, a relativistic and a Skyrme EDF parameterization (DD-ME δ , SAMi-J28) of the Ref. [40]. Δ NNLO is the chiral EFT interaction recently proposed by explicitly including Δ -isobar [22]. NNLO $_{\text{sat}}$ and DD-ME δ give reasonable r_p values while Δ NNLO and SAMi-J28 predict larger r_p and r_n . However, for the skin thickness of ^{48}Ca , all the predictions give consistent values with our result considering the error.

Figure 3 compares the experimentally-determined density distributions in ^{48}Ca (red solid and hatched lines) with the predictions by NNLO $_{\text{sat}}$ (blue short-dash), Δ NNLO (magenta long-dash), DD-ME δ (green dash-dotted), and SAMi-J28 (black dotted). The lower panel (b) of Fig. 3 shows the deviations of each prediction from our prediction by $4\pi r^2$ ($\Delta = 4\pi r^2(\rho^{\text{cal}} - \rho^{\text{exp}})$). For clarity, ρ_n and Δ_n are shifted by $+0.02 \text{ fm}^{-3}$ and $+1.0 \text{ fm}^{-1}$, respectively. The NNLO $_{\text{sat}}$ and DD-ME δ predictions surprisingly agree with our result. Δ NNLO and SAMi-J28 predict large diffusenesses of ρ_p and ρ_n . Consequently, they give larger r_p and r_n , compared to our work. It is thus demonstrated that comparison with the experimentally obtained ρ_p and ρ_n enables the assessment of the theoretical predictions which is not possible only with the neutron skin thickness. This is an advantage in the proton elastic

scattering method over other methods that determine only the radii or skin thicknesses.

The obtained values of Δr_{np} in $^{40,48}\text{Ca}$ with the experimental errors are $-0.010^{+0.022}_{-0.024} \text{ fm}$ and $0.168^{+0.025}_{-0.028} \text{ fm}$, respectively. The ^{40}Ca result is consistent with almost all the theoretical calculations, which predict a small proton skin in ^{40}Ca . The small proton skin is a result of the repulsive Coulomb force that pushes protons outwards. The result of Δr_{np} in ^{48}Ca is consistent in the range of 0.14–0.20 fm, which was recently obtained by interpreting the dipole polarizability (DP) of ^{48}Ca [26]. However, the value of $\Delta r_{np} = 0.249(23) \text{ fm}$ reported by the dispersive optical model (DOM) analysis [41] differs from our work and the DP result. The left panel of Fig. 4 plots the correlation between Δr_{np} in ^{48}Ca and the slope parameter L of the symmetry energy predicted by the *ab initio* and EDF models, while the right panel compares the Δr_{np} values of ^{48}Ca and ^{208}Pb predicted by the relativistic and Skyrme EDF models. Black squares, green triangles, and magenta circles represent the predictions of the *ab initio* method, the relativistic EDF models (NL3 [42], DD-ME2 [43] DD-ME δ [44], DD-PC1 [45], FSU [46], FSU2 [47] IUFSU [48]) and Skyrme EDF models (SkM* [49], Sk255, Sk272 [50], SeaLL1 [51], UNEDF0 [52]), respectively. Open triangles and circles are sets of the DD-ME and SAMi-J families in Ref. [40], respectively. Open squares are the *ab initio* results by newly developed NNLO $_{\text{sat}}$ and Δ NNLO interactions. The blue rectangle represents the region estimated from several chiral EFT interactions by G. Hagen *et al.* in Ref. [25]. The red hatched area shows the result of our work while the arrows are the ranges by DP and DOM analyses. Compared to the recent EDF theories, *ab initio* theories predict a slightly smaller neutron skin thickness. Our result for ^{48}Ca implies that L is in the range of 20–70 MeV. The right panel of Fig. 4 plots the correlation between the ^{48}Ca and ^{208}Pb skin thicknesses. A difference between the results from the proton elastic scattering and from the dipole polarizability is noticeable. The arrow denotes the PREX result of ^{208}Pb [15].

In summary, we performed a direct determination of the neutron density distributions and the skin thicknesses of $^{40,48}\text{Ca}$ from proton elastic scattering at 295 MeV. The obtained value of $\Delta r_{np} = 0.168^{+0.025}_{-0.028} \text{ fm}$ for ^{48}Ca is consistent with the DP analysis, while the DOM analysis provides a large skin thickness. The recent *ab initio* and EDF predictions give consistent values of Δr_{np} with this work. In particular, the calculations of the *ab initio* CC model using the NNLO $_{\text{sat}}$ interaction and the DD-ME δ model provide density distributions that are consistent with our result.

We would like to express our gratitude to the RCNP accelerator group for providing the high-quality beam. This work was in part supported by JSPS KAKENHI Grant Number 15H05451, the U.S. Department of Energy, Office of Science, Office of Nuclear Physics under Award Number de-sc0018223 (SciDAC-4 NUCLEI), and the Field Work Proposals ERKBP57 and ERKBP72 at Oak Ridge National Laboratory (ORNL). Computer time was provided by the Innovative and Novel Computational Impact on Theory and Experiment

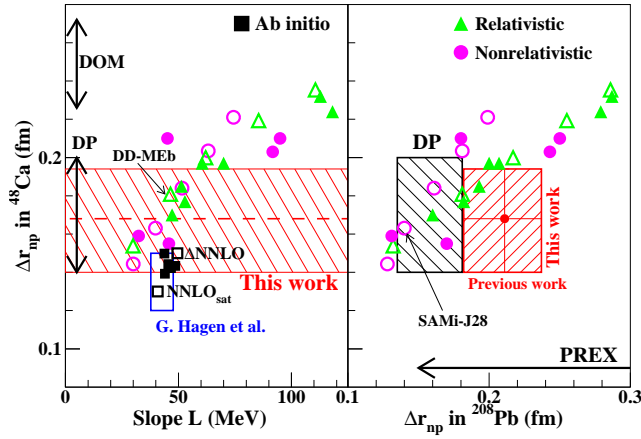


FIG. 4. (Left) Δr_{np} in ^{48}Ca versus the slope parameter L . (Right) Δr_{np} in ^{48}Ca versus ^{208}Pb . Squares, triangles, and circles are predictions by *ab initio* CC method with chiral EFT interactions, relativistic and Skyrme EDFs, respectively. In the left panel, the arrows indicate the result of DP and DOM analyses, while the present result is shown by a red dash line with the hatched area. The blue rectangle shows the region evaluated in Ref. [25]. In the right panel, the red hatched region shows the overlap between this work for ^{48}Ca and the previous work for ^{208}Pb of Ref. [11]. The arrow is due to the PREX experiment, while the black hatched region is obtained by the DP analyses.

(INCITE) program.

* juzu@ribf.riken.jp

[1] M. Oertel, *et al.*, Rev. Mod. Phys. **89**, 015007 (2017).
 [2] D. Radice, *et al.*, Astrophys. J. **852**, L29 (2018).
 [3] X. Roca-Maza and N. Paar, Prog. Part. Nucl. Phys. **101**, 96 (2018).
 [4] F. J. Fattoyev, J. Piekarewicz, and C. J. Horowitz, Phys. Rev. Lett. **120**, 172702 (2018).
 [5] E. Annala, *et al.*, Phys. Rev. Lett. **120**, 172703 (2018).
 [6] B. P. Abbott, *et al.*, Phys. Rev. Lett. **119**, 30 (2017).
 [7] S. Typel and B. A. Brown, Phys. Rev. C **64**, 027302 (2001).
 [8] R. J. Furnstahl, Nucl. Phys. A **706**, 85 (2002).
 [9] L.-W. Chen, C. M. Ko, and B.-A. Li, Phys. Rev. C **72**, 064309 (2005).
 [10] V. E. Starodubsky and N. M. Hintz, Phys. Rev. C **49**, 2118 (1994).
 [11] J. Zenihiro, *et al.*, Phys. Rev. C **82**, 44611 (2010).
 [12] C. M. Tarbert, *et al.*, Phys. Rev. Lett. **112**, 242502 (2014).

[13] B. Klos, *et al.*, Phys. Rev. C **76**, 014311 (2007).
 [14] A. Tamii, *et al.*, Phys. Rev. Lett. **107**, 1 (2011).
 [15] S. Abrahamyan, *et al.*, Phys. Rev. Lett. **108**, 112502 (2012).
 [16] X. Roca-Maza, *et al.*, Phys. Rev. Lett. **106**, 252501 (2011).
 [17] M. B. Tsang, *et al.*, Phys. Rev. C **86**, 015803 (2012).
 [18] R. J. Furnstahl and K. Hebeler, Reports Prog. Phys. **76**, 126301 (2013).
 [19] V. Somà, *et al.*, Phys. Rev. C **89**, 061301 (2014).
 [20] A. Ekström, *et al.*, Phys. Rev. C **91**, 051301 (2015).
 [21] H. Hergert, *et al.*, Phys. Rep. **621**, 165 (2016).
 [22] A. Ekström, *et al.*, Phys. Rev. C **97**, 024332 (2018).
 [23] A. Akmal, V. R. Pandharipande, and D. G. Ravenhall, Phys. Rev. C **58**, 1804 (1998).
 [24] G. Hagen, *et al.*, Phys. Scr. **91**, 063006 (2016).
 [25] G. Hagen, *et al.*, Nat. Phys. **12**, 186 (2015).
 [26] J. Birkhan, *et al.*, Phys. Rev. Lett. **118**, 252501 (2017).
 [27] C. J. Horowitz, K. S. Kumar, and R. Michaels, Eur. Phys. J. A **50**, 48 (2014).
 [28] S. Terashima, *et al.*, Phys. Rev. C **77**, 024317 (2008).
 [29] M. Fujiwara, *et al.*, Nucl. Instruments Methods Phys. Res. Sect. A Accel. Spectrometers, Detect. Assoc. Equip. **422**, 484 (1999).
 [30] H. Sakaguchi and J. Zenihiro, Prog. Part. Nucl. Phys. **97**, 1 (2017).
 [31] D. P. Murdock and C. J. Horowitz, Phys. Rev. C **35**, 1442 (1987).
 [32] C. J. Horowitz, Phys. Rev. C **31**, 1340 (1985).
 [33] H. Sakaguchi, *et al.*, Phys. Rev. C **57**, 1749 (1998).
 [34] H. De Vries, C. De Jager, and C. De Vries, At. Data Nucl. Data Tables **36**, 495 (1987).
 [35] C. J. Horowitz and B. D. Serot, Nucl. Physics, Sect. A **368**, 503 (1981).
 [36] K. Nakamura, *et al.*, J. Phys. G Nucl. Part. Phys. **37** (2010).
 [37] H. Kurasawa and T. Suzuki, Phys. Rev. C **62**, 054303 (2000).
 [38] C. J. Horowitz and J. Piekarewicz, Phys. Rev. C **86**, 045503 (2012).
 [39] W. Bertozzi, *et al.*, Phys. Lett. B **41**, 408 (1972).
 [40] X. Roca-Maza, *et al.*, Phys. Rev. C **87**, 034301 (2013).
 [41] M. H. Mahzoon, *et al.*, Phys. Rev. Lett. **119**, 222503 (2017).
 [42] G. a. Lalazissis, J. König, and P. Ring, Phys. Rev. C **55**, 540 (1997).
 [43] G. A. Lalazissis, *et al.*, Phys. Rev. C **71**, 024312 (2005).
 [44] X. Roca-Maza, *et al.*, Phys. Rev. C **84**, 054309 (2011).
 [45] T. Nikšić, D. Vretenar, and P. Ring, Phys. Rev. C **78**, 034318 (2008).
 [46] B. G. Todd-Rutel and J. Piekarewicz, Phys. Rev. Lett. **95**, 1 (2005).
 [47] W.-C. Chen and J. Piekarewicz, Phys. Rev. C **90**, 044305 (2014).
 [48] F. J. Fattoyev, *et al.*, Phys. Rev. C **82**, 055803 (2010).
 [49] J. Bartel, *et al.*, Nucl. Phys. A **386**, 79 (1982).
 [50] B. K. Agrawal, S. Shlomo, and V. Kim Au, Phys. Rev. C **68**, 031304 (2003).
 [51] A. Bulgac, *et al.*, Phys. Rev. C **97**, 044313 (2018).
 [52] M. Kortelainen, *et al.*, Phys. Rev. C **82**, 024313 (2010).